Simultaneous 100-kHz acetone planar laser-induced fluorescence and OH* chemiluminescence in a linear non-premixed detonation channel

Zachary M. Ayers[a], Aaron Lemcherfi[b], Ethan W. Plaehn[b], Rohan M. Gejji[b], H. Douglas Perkins[d], Sukesh Roy[c], Carson D. Slabaugh[b,*], Terrence R. Meyer[a,b,*], Christopher Fugger[c,*]

[a] *School of Mechanical Engineering, Purdue University, West Lafayette, IN 47907, USA*
[b] *School of Aeronautics & Astronautics, Purdue University, West Lafayette, IN 47907, USA*
[c] *Spectral Energies LLC, Beavercreek, OH, 45430, USA*
[d] *NASA Glenn Research Center, Cleveland, Ohio 44135, USA*

Abstract

Reactant mixing and combustion are investigated in an optically accessible, self-excited linear detonation combustor. The mixing field is captured using 100 kHz planar laser-induced fluorescence (PLIF) imaging of acetone as a tracer in the fuel supply, while 100 kHz chemiluminescence imaging of excited-state hydroxyl (OH*) radicals simultaneously resolves the evolution of the detonation wave. Time sequences are acquired over multiple detonation cycles in each test, with acetone-PLIF images collected along multiple orthogonal planes to reveal the complex three-dimensional topography of the fuel distribution. The instantaneous and phase-averaged acetone-PLIF images enable measurement of key fuel injection characteristics, such as the injector recovery time, fuel jet velocity, and refill height for a range of operating conditions. Instantaneous and phase-averaged measurements of acetone-PLIF with the time-coincident OH* chemiluminescence images also reveal a number key features, such as fuel stratification and weak detonation in the injector near field, incomplete combustion and deflagration behind the detonation wave, vitiation and deflagration of reactants ahead of the detonation wave, and fuel and oxidizer recovery time mismatch leading to combustion inefficiency. These measurements significantly enhance the ability to obtain detailed information on the intracycle and intercycle spatiotemporal evolution of the reactant refill process and its coupled effects on the detonation wave structure and propagation.

Keywords: Linear detonation combustor, rotating detonation engine, rotating detonation combustor, planar laser-induced fluorescence, reactant mixing, OH* chemiluminescence

1. Introduction

As significant improvements in gas turbine and rocket propulsion technologies are sought [1, 2], the propulsion community has turned to pressure-gain combustion (PGC) as a potential technology for achieving a step change in system performance. The simple, compact architecture and continuous cycle operation inherent to the rotating detonation combustor (RDC), or rotating detonation engine (RDE), makes it a particularly appealing replacement to traditional deflagration-based combustors. The RDE supports a detonation-based cycle wherein chemical kinetic processes occur on much smaller timescales than gas expansion processes. The high reaction rates at the detonation front result in approximately constant-volume combustion and higher combustion pressures. Thermodynamic analyses using this combustion mechanism show potential efficiency advantages over deflagrative combustion cycles via increased energy extraction with improved thermal power density [3, 4].

However, RDE development has been constrained by a lack of understanding of the short-timescale intracycle processes that determine global operability and performance. One of the most significant uncertainties is the effect of the reactant mixing field on detonation wave behavior. Premixed RDE simulations generally overpredict detonation wave velocities observed in non-premixed experiments [5], indicating that reactant mixing has a significant impact on the detonation cycle. Meanwhile, non-premixed simulations note varying effects of mixing on wave speed [6–9]. Non-premixed simulations have also observed the emergence of shock structures that form in the wake of the detonation wave, creating secondary heat release zones as the shocks travel through the mixture behind the wave [7, 10–13]. These studies confirmed that heat release behind the detonation wave is indicative of incomplete combustion at the detonation front due to poor mixing. Poor mixing near the injector face was also shown to result in forward-leaning and even lifted detonation waves–phenomena that have also been observed in experiments [14, 15]. Thus, the mixing process has pronounced effects on chamber dynamics and the need to understand these effects is clear.

Deflagrative burning in the refill zone is another related facet of the detonation cycle with an unquantified impact on combustor performance. Premixed RDE experiments have produced wave velocities that fall short of expected C-J velocities and partial combustion of reactants prior to wave arrival has been proposed as a possible explanation [5, 16]. Simula-

---

tions have shown deflagration in the refill zone to lower wave speeds and even cause the detonation cycle to fail [6, 8]. Stechmann et al. similarly noted that excess deflagration was likely the cause of detonation failure in a rotating detonation rocket engine (RDRE) experiment and emphasized the importance of mixing and ignition delay time in determining the level of deflagrative burning [17]. Water temperature measurements in the chamber of another RDRE estimated the mass fraction of combustion products in the refill zone to be as high as 20-30% in some cases [18]. Given these proposed impacts of refill zone deflagration on cycle efficiency, wave speed, and combustor operability, further study is required to understand the effects of refill zone deflagration and the factors that contribute to it.

Another aspect of the reactant mixing process that has yet to be adequately characterized is the injector recovery time–defined as the period during which reactant supply is cut off at the injector after detonation wave passage. It has been theorized that injector recovery times play a role in determining cycle frequency and that long recovery times may induce unpredictable wave dynamics and local equivalence ratio fluctuations [19–22]. In addition, the recovery time has design implications for determining detonation wave height and combustor length. Results from Sato, et al. also suggested that a mismatch in recovery times between the fuel and oxidizer may produce regions of extreme mixture ratios, incapable of reacting before being ejected from the chamber [23]. However, no recovery time measurements were made to support their hypothesis. In another study, injector recovery time in an RDE was experimentally measured for the first time and it was directly confirmed that fuel injection can be temporarily halted following detonation wave passage [24]. However, the 10 Hz measurement rate did not allow for resolution of any single detonation cycle and the study produced only phase-averaged results. Thus, further recovery time data is required to improve understanding of the refill process and to inform engine designs.

Therefore, with this understanding of the controlling impact of reactant refill dynamics on RDE behavior, it is clear that a full characterization of the physics at play demands a thorough examination of reactant injection and mixing processes. However, RDE flowfield imaging studies have generally focused on capturing detonation wave characteristics [14, 15, 23, 25–28]. Experiments conducted in linear detonation channels have similarly placed emphasis on the evolution of detonation wave structure with various injection schemes [29–31]. Non-reacting imaging studies of fuel distribution have been performed in configurations designed to imitate RDE environments [32–34], providing useful information without the complex dynamics present in RDEs. The only previous experimental visualization of the reactant mixing field in a detonation combustor was presented in the aforementioned study from Rankin, et al [24]. The authors performed 10-Hz-rate planar laser-induced fluorescence (PLIF) measurements of acetone vapor in the fuel supply to image the fuel distribution [24]. Due to the annular combustor geometry and the injection scheme, the field of view was restricted and a more comprehensive analysis is needed to fully address the impact of the mixing process.

Thus, the limited experimental evidence surrounding the evolution of the mixing field in detonation engines necessitates further study. In a recent conference paper, the current authors demonstrated preliminary work on intracycle resolution of the reactant refill process in a linear detonation combustor using 100 kHz acetone-PLIF [35]. The study served to demonstrate the capability of the diagnostic and to reveal the general refill process, but the lack of heat release data limited conclusions that could be drawn regarding the relationship between refill and detonation wave dynamics. In the current work, we address the need for high-speed diagnostic measurements capable of spatially and temporally resolving the evolution of both the mixing field and heat release zones within multiple detonation cycles. To this end, simultaneous 100 kHz acetone-PLIF and OH* chemiluminescence imaging techniques are performed in a self-excited, linear detonation combustor to simultaneously capture the mixing field and combustion characteristics. The combustor produces fully developed detonation waves in an optically accessible environment at kHz frequencies to emulate reactant injection and combustion dynamics found in annular RDEs. Key features of the mixing process are observed within the detonation and post-detonation environments, including the reactant refill rate and recovery time as a function of operating conditions, vitiation and deflagrative burning of the reactants, unburned reactants behind the detonation wave due to poor mixing in the injector near field, and poor combustion due to fuel-oxidizer recovery time mismatch in the injector far field. These observations highlight the utility of simultaneous 100 kHz fuel-tracer PLIF and OH* chemiluminescence for providing more detailed information on the coupled interactions between the mixing field and detonation wave characteristics.

2. Experiment Description

2.1. Linear Detonation Channel

Experiments were performed in the linear detonation combustor illustrated in Fig. 1. A detailed discussion of the design and self-excited behavior of the test article is presented in [26]. A channel measuring 7.62 mm wide, 91 mm high, and 610 mm long forms the combustion chamber. Gaseous supplies of oxygen and natural gas are injected in the $+x$ direction from below the $x=0$ plane relative to the coordinate system defined in Fig. 1. The top of the chamber and the $+y$ exit boundary are open to ambient conditions. The $y=0$ boundary is enclosed by a stainless steel plate which provides a mounting location for the ignition device. The oxidizer injector consists of a 0.76 mm wide slot that spans the (y-direction) length of the chamber and is centered between the chamber walls. The fuel injection scheme incorporates 1.27 mm diameter orifices, distributed on alternating sides of the oxidizer slot along the full length of the combustion chamber. Each fuel injector introduces fuel at an angle of 30° relative to the $+x$-axis. Ports on either side of the chamber allow for fused quartz windows for optical access or metal blanks wherein traditional pressure instrumentation can be installed. In the present work, metal blanks were installed in the Window A position on both sides of the channel and quartz windows were installed in the Window B position on both sides, as
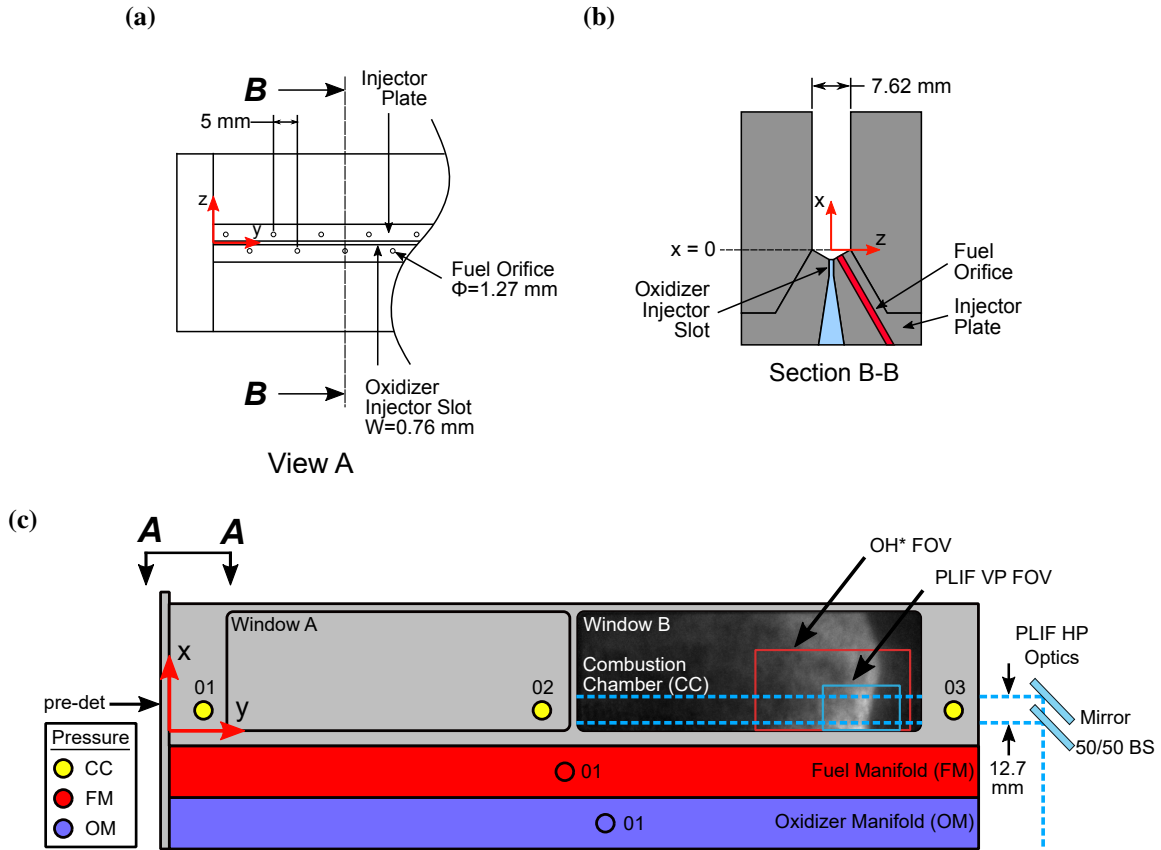
Figure 1: (a) Top view of injector plate, (b) test article cross-section through fuel orifice, and (c) side view detailing window and instrumentation port locations. BS - beam splitter, HP - horizontal plane, VP - vertical plane, FoV - field of view.

shown in Fig. 1(c). To initiate the combustion process, a spark-ignited H_2-O_2 predetonator is used as an ignition source at the y=0 end after reactants reach a steady state in their respective manifolds. Following ignition, the unique chamber and manifold dynamics in the combustor create self-sustained detonation waves at a rate of 6-12 kHz (depending on combustor operating conditions) that propagate along the length of the combustor (y-direction).

2.2. Acetone Seeding System

In this study, acetone is used as a fuel flow tracer that has the added benefit of decomposing (i.e. pyrolysis) at elevated temperatures, thus helping to serve as an isotherm in the complex detonation environment. Acetone has been employed as an effective tracer for mixture fraction and temperature imaging in reacting and non-reacting flows [36–40]. In an isothermal environment, the linear relationship between excitation energy and fluorescence yield creates a simple conversion from fluorescence intensity to mixture fraction, provided reference values of intensity and mixture fraction can be obtained [41]. An inverse relationship between temperature and fluorescence yield was documented by Thurber et al. [42], revealing that acetone fluorescence drops to less than 10% of its room temperature value at 1000 K under 266 nm excitation. Above 1000 K, acetone decomposes due to pyrolysis, significantly reducing

the acetone mole fraction. Thus, without any temperature correction, the acetone fluorescence signal will quickly diminish in the vicinity of a flame. In the absence of local measurement of gas temperature in this study, no corrections for temperature were performed and the PLIF images provide a qualitative assessment of fuel distribution prior to periodic consumption by the detonation wave. The images further serve to indicate where reactions may be taking place. In another study, Thurber and Hanson documented the relative insensitivity of acetone vapor fluorescence to changes in pressure [41]. Their study showed that fluorescence intensity only varied by ~10% from pressures of 0.5 to 8 atm under 266 nm excitation in an oxygen bath gas. Oxygen quenches the fluorescence that would otherwise increase with pressure, resulting in a nearly constant fluorescence yield. Thus, the acetone fluorescence signal is mainly a function of temperature, mixture fraction, and excitation energy after mixing with oxygen in the experiment.

An acetone vapor delivery system was developed to ensure precise metering of acetone as a tracer for the fuel. This allowed for the effects of acetone to be replicated in a precise fashion irrespective of the high amplitude combustion dynamics in the chamber and hydrodynamics in the fuel manifold. Accurate metering of acetone ultimately permitted the characterization of the spatial fuel distribution across a range of operating conditions. Several previous combustion studies have

3

employed bubbler tanks to entrain acetone vapor into the fuel supply [24, 40, 43–46]. However, to estimate the acetone mass fraction in the fuel, this method requires an assumption that the acetone exists as a saturated vapor which is not always accurate in practice [43]. In this work, acetone is introduced into the flow of natural gas at the target pressure and flow-rate by free-surface pressurization in a tank using an inert gas. The mass flow rate of acetone is metered using a cavitating venturi. Prior to acetone addition, natural gas flows through a 4.4 MJ pebble bed heater, described in [35], to allow for acetone vaporization at fuel manifold pressures. The tubing downstream of the heater is wrapped in heat tape to reduce heat transfer to the tube walls. Once the fuel exits the heater, acetone is injected into the flow and the mixture continues directly to the experiment.

2.3. Instrumentation and Measurements

High-frequency pressure measurements were acquired at the locations shown in Fig. 1(c) to characterize chamber dynamics throughout each test. Piezoelectric pressure transducers (PCB 113B26), sampled at 2 MHz, were installed flush with the chamber walls to measure dynamic pressure in the experiment. Static pressures in the propellant manifolds and combustion chamber were measured at 2 MHz using piezoresistive pressure transducers (Kulite WCT312M). Gaseous flow rate monitoring was achieved using pressure transducers (GE-UNIK 50E6) and Omega type-K thermocouples immediately upstream of critical flow venturi nozzles (CFVN) that conform to ISO 9300 specifications. The pressure drop across each CFVN was monitored to ensure a choked condition throughout the test duration despite the highly dynamic processes occurring downstream.

An Nd:YAG burst-mode laser (Spectral Energies, Quasimodo) was used as the acetone excitation source, frequency quadrupled to produce 266 nm pulses at 100 kHz, each with a 12 ns pulsewidth. Figure 2(a) provides a schematic of the optical layout. Acetone PLIF was performed in multiple planes, as illustrated in Fig. 2(b). For measurements in the vertical plane (VP1), a 38 mm tall laser sheet was formed using a -100 mm cylindrical lens, a +500 mm cylindrical lens, and a +1000 mm spherical lens. Since the laser pulse energy scales inversely with the burst width, the laser burst width was set to 1.5 ms in order to maximize the ratio of fluorescence signal to background flame luminosity. This resulted in 150 pulses at an average pulse energy of 17 mJ. A Phantom v2012 high-speed CMOS camera was coupled to a high-speed Lambert HiCatt intensifier (GaAsP) and equipped with a Nikon 200 mm f/8 visible lens for acetone-PLIF imaging. A bandpass filter (Semrock FF01-439/154) was used to isolate the acetone fluorescence and to eliminate flame luminosity. An additional 266 nm longpass filter (Edmund Optics #12-255) was installed to remove spurious scattered laser light from the images. The intensifier gate was set to 20 ns to reduce background flame luminosity. The PLIF imaging system provided a 320x512 pixel array with a field-of-view mapping of 95 μm/pixel on the camera sensor. The camera and intensifier were positioned parallel to the channel and viewed the test section via a broadband mirror. The field of view (FoV) was positioned ~20 mm from the +y edge

of window B. This FoV was selected to minimize laser attenuation between the open end of the chamber and the FoV and to ensure that the detonation waves passing through the FoV were fully developed.
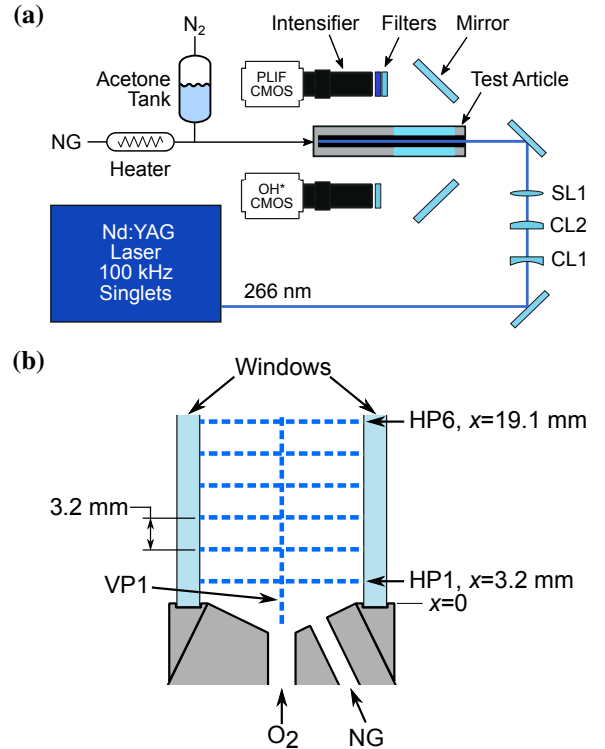

Figure 2: (a) Optical layout and (b) cross-section of linear detonation channel illustrating laser sheet locations. CL - cylindrical lens, SL - spherical lens, NG - natural gas, HP - horizontal plane, VP - vertical plane.

For horizontal (HP1-HP6) plane measurements, a +400 mm lens was substituted in the CL2 position and a 50/50 beamsplitter was installed ahead of the final turning mirror, as illustrated in Fig. 1(c). This arrangement produced two parallel 8 mm wide laser sheets with a 12.7 mm spacing in the x-direction. The camera, intensifier, and viewing mirror were elevated above the combustor to achieve a vantage point from which to view both horizontal planes in the same FoV. The x-positions of the final turning optics and of the camera and intensifier were set using synchronized translation stages. This allowed for measurements to be made in several planes in successive tests while the y- and z-coordinates of the FoV were maintained. This configuration provided a spatial resolution of 140 μm/pixel in the z-direction and 150 μm/pixel in the y-direction after the images were deskewed in post-processing. The HP1 plane was positioned 3.2 mm above the top of the injector plate, and a 3.2 mm spacing was maintained between neighboring laser sheet positions. The reduced laser sheet size required for horizontal plane measurements rendered a higher fluence, so a 2.5 ms burst duration could be used, resulting in 250 pulses with an average pulse energy of 8.3 mJ for each laser sheet.

Chemiluminescence imaging was performed along with the PLIF imaging in both arrangements using a Phantom v2512

4

high-speed CMOS camera coupled to a high-speed Lambert HiCatt intensifier (S20) with a 1 μs gate and a Nikon 100 mm f/2.8 UV lens. A bandpass filter (Semrock FF02-320/40) was installed to isolate the OH* chemiluminescence signal. Images were captured in a 320x512 pixel array with 198 μm/pixel resolution. To ensure that no acetone-PLIF signal or scattered laser light was captured in the chemiluminescence images, the intensifier gate was set to end 20 ns before the start of the PLIF intensifier gate. Detonation waves were found to move less than one pixel on either camera during this temporal offset. The chemiluminescence FoV encapsulated the PLIF FoV and was large enough to provide insight into detonation wave structures just before the wave entered the PLIF FoV. Like the PLIF camera, the OH* chemiluminescence camera was positioned parallel to the channel and viewed the test section via a broadband mirror. Spatial calibration images were acquired using a two-sided dual plane dot target (LaVision 058-5) so that the FoVs could be spatially correlated in post-processing. The images were processed through the LaVision DaVis software for spatial calibration and image registration. For the horizontal plane measurements, the PLIF camera was spatially calibrated using a custom-made dot target that could be positioned at the plane of interest. The calibration images were then also spatially corrected using the DaVis software.

2.4. Combustor Operation

Reactant manifolds were primed with O_2 and natural gas (with acetone) prior to chamber ignition from the pre-detonator at t=0 s. As shown in Fig. 3, limit-cycle combustor operation characterized by the generation of periodic steep-fronted pressure waveforms was observed within 2 ms of chamber ignition. Chemiluminescence images were acquired throughout the test beginning ~12 ms after ignition. Both the laser and the acetone-PLIF camera were triggered 60 ms after the predetonator spark. Due to the high thermal power of the combustor and lack of active cooling measures, the test duration was limited to ~0.25 s. This was sufficient to observe statistically-stationary combustor dynamics at the frequencies of interest in the experiment. At the end of this period the reactant supply valves were closed and the fuel and oxidizer flows were replaced with an inert purge.

2.5. Experimental Conditions

The experimental operating conditions employed in this study are given in Table 1. To study reactant refill and combustion dynamics, three test cases (Cases A, C, and D) with differing equivalence ratios (ϕ), but similar total reactant mass flow rates ($\dot{m}_{total}$), were investigated, where $\dot{m}_{total}$ is the summation of the oxidizer ($\dot{m}_{ox}$), fuel ($\dot{m}_{fuel}$), and acetone seed ($\dot{m}_{seed}$) mass flow rates. Additionally, to determine the effects of fuel seeding on detonation performance, two of the cases were repeated without acetone addition to the fuel (Cases B and E). The chamber mass flux, $G_{chamber}$, is calculated as the total mass flux of all reactants through the y–z cross-section of the chamber. The % Seed (Mass) is the acetone mass fraction in the acetone/natural gas fuel mixture. For cases with acetone addition, an acetone mass fraction of roughly 10% of the total fuel
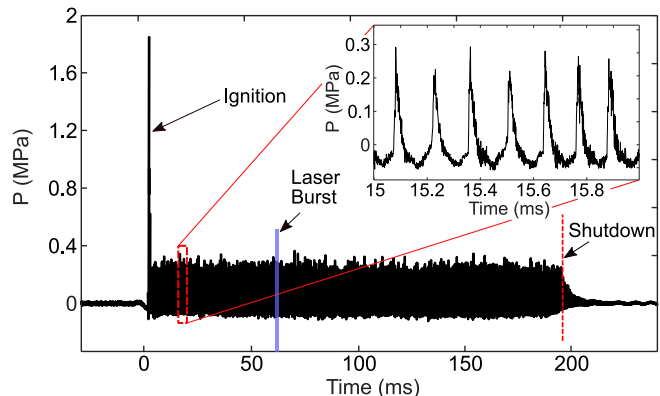

Figure 3: Dynamic pressure-time history of a representative test measured at location CC-03.

mixture was selected. This level was chosen to maximize fluorescence signal while minimizing potential effects on chamber dynamics. The use of the pebble bed heater resulted in elevated fuel manifold temperatures (T_{FM}). However, these cases revealed no significant changes in detonation wave frequency or average chamber pressure fluctuations (P') when compared to tests run without heat addition to the fuel. The oxygen manifold temperatures (T_{OM}) were stable and below ambient temperature due to expansion cooling.

The frequency of detonation wave passage (f) is calculated by extracting the dominant frequency mode of the pressure measured at the CC-03 position from the time that stable operation is achieved until shutdown. Schwinn et al. [26] suggest that the wave generation frequency in this combustor generally corresponds to the frequency of the acoustic modes in the reactant manifolds. When the ratio of fuel manifold pressure to oxidizer manifold pressure is above 1.2, the detonation wave frequency transitions from the frequency of the highest amplitude acoustic mode of the oxidizer manifold to that of the fuel manifold. This results in an increase in the wave generation frequency at an equivalence ratio near unity where the fuel manifold pressure becomes higher than that of the oxidizer manifold (hence why Cases C, D, and E have higher f compared to Cases A and B). Note that unlike an RDE, the frequency measured in this linear combustor is not inherently tied to detonation wave speed and chamber geometry. Each wave is independently generated and amplified and transitions to a detonation before propagating out of the channel.

Comparisons of average detonation wave generation frequencies and P' values indicate that the trace amounts of acetone seeded into the fuel flow have a negligible effect on combustor operation. Here, P' is calculated by subtracting the average cycle minimum pressure from the average cycle peak pressure. Comparisons of Cases A and B as well as D and E show that f from tests with and without acetone addition, respectively, lie within 1.7% of each other. Although the average pressure fluctuations do show greater variation across these test cases, the data do not support a clear trend as P' decreases without acetone addition from Case A to Case B but increases from Case D to Case E. To further investigate the effects of the fuel

5

Table 1: Summary of operating conditions.

Case	ϕ	$\dot{m}_{ox}$ (kg/s)	$\dot{m}_{fuel}$ (kg/s)	$\dot{m}_{seed}$ (kg/s)	$\dot{m}_{total}$ (kg/s)	$G_{chamber}$ (kg/s.m²)	% Seed (Mass)	f (kHz)	P' (kPa)	T_{OM} (K)	T_{FM} (K)
A	0.83	0.46	0.09	0.010	0.56	121	9.7	6.6	285	286	318
B	0.81	0.46	0.09	0	0.55	121	0	6.7	263	285	320
C	0.97	0.43	0.10	0.012	0.55	117	10.8	10.6	298	285	350
D	1.26	0.41	0.12	0.015	0.55	119	10.6	10.6	243	286	348
E	1.28	0.41	0.13	0	0.54	119	0	10.7	275	284	335

tracer, the average position of the leading edge of the detonation wave front was calculated for Cases A, B, D, and E using Sobel edge detection [47]. In every case, the average profile of the wave front was computed using 1500 images captured over a 15 ms time interval. These results are shown in Figure 4. Cases A and B show minimal difference in the average wave front. Cases D and E also display separation of less than 1 mm below x=40 mm, above which Case E shows a greater oblique shock angle. Additional contributions leading to this difference may include (*i*) differences in P' (Table 1) between the test cases and (*ii*) the representation of an inherently three-dimensional wave structure with the path integrated nature of the chemiluminescence imaging. Thus, tests conducted with acetone addition are representative of typical combustor operation.
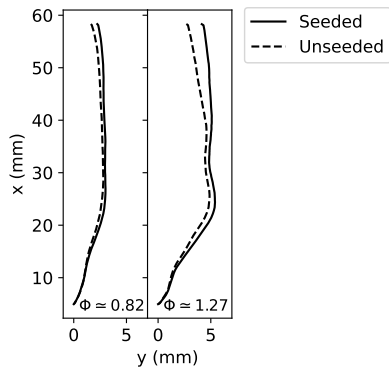

Figure 4: Average detonation front profiles from cases A and B (left) and D and E (right) revealing minimal impact on the detonation wave structure due to acetone addition (y-axis scale is twice that of the x-axis to highlight variations in the wave profiles).

3. Results and Discussion

Both qualitative and quantitative results are presented in this section. First, the fuel mixing fields from the acetone-PLIF images are shown along the different cross-sectional measurement planes and their spatio-temporal characteristics are discussed. Next, the OH* chemiluminescence imaging is presented and discussed, followed by presentation and characterization of the phased-averaged combustion (from OH*) and fuel mixing (from acetone PLIF) fields. Following that, the fuel injection recovery times are quantified along with the fuel jet velocities.

3.1. Instantaneous Fuel Injection Characteristics

Given the importance of the reactant refill process in driving detonation dynamics, the validity of computational models relies on accurate predictions of this process. However, little experimental evidence exists to evaluate these predictions or more generally to characterize the reactant mixing. To address these needs, this section presents spatially and temporally resolved cross-sectional images of the fuel refill and mixing processes on an instantaneous and phase-averaged basis.

A representative time series of vertical plane acetone-PLIF images for Case D is shown in Fig. 5, displaying a complete cycle of the fuel mixing field with passage of the detonation wave. Here, all images are normalized to the maximum intensity value in the time series. For these images and all that follow, a mean background subtraction has been applied. The image series begins at 61.62 ms with the fuel refill process well underway. Near the injector, individual fuel streams are readily observed and it is noted that ten fuel orifices (denoted by the red arrows at 61.70 ms) are located inside the PLIF FoV. The compact fuel streams and relatively high PLIF signal suggest the fuel jets are not well mixed close to the injector. Further downstream (*x*-direction), the fuel streams become less distinguishable and the fuel becomes more spatially homogeneous and mixed with surrounding gases.

A detonation wave is present in the FoV from 61.65–61.68 ms (denoted by a nearly vertical dotted line, moving left to right) and can be recognized by low-level flame luminosity at the detonation front. As the detonation wave propagates past a particular location, surviving fuel jet structures observed behind the wave indicate that pockets of high fuel concentration are not fully consumed at the detonation front. The frames from 61.67–61.69 ms reveal that before these pockets of fuel are fully consumed, they detach from the injector face, indicating that the fuel injector pressure has been overcome and that the inflow of freshly injected fuel into the combustor has temporarily halted. These small regions of fuel are eventually consumed by a trailing zone of heat release behind the detonation front, as later indicated by OH* chemiluminescence measurements.

After a fuel jet recovery time following passage of the detonation wave, the inflow of fuel into the chamber is again observed. The fuel jet heights form an upward slope (refer to the refill slope dotted line at 61.70 ms), with the fuel jet height furthest from the previous detonation wave being larger. Also observed is a lean of the fuel jets in the +y-direction when first entering the combustor. This is apparent at 61.70 ms where recovering fuel jets first favor the +y side of their injection loca-
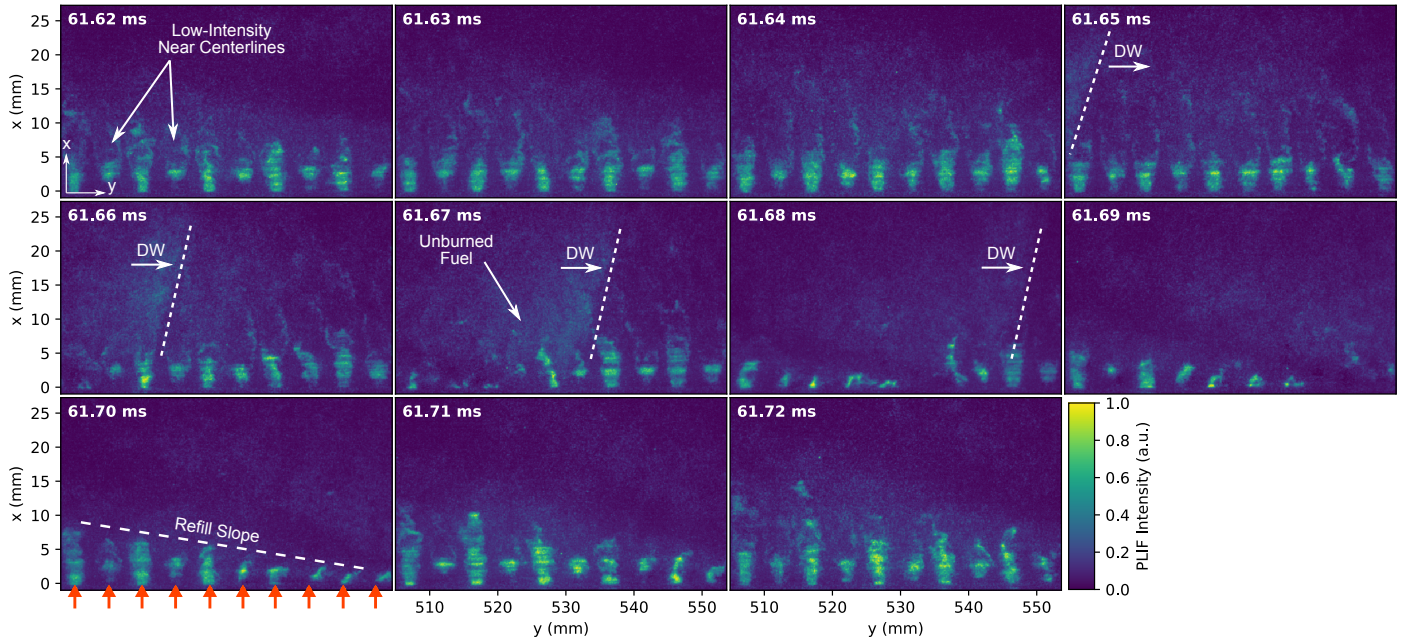
Figure 5: Vertical plane acetone-PLIF images from a single detonation cycle during a test at Case D operating conditions (detonation propagation is left to right). DW - detonation wave.

tions (denoted by the arrows), but gradually become centered. This behavior is not unexpected in the expansion region behind the detonation wave as it highlights the contact with combustion products of the previous wave. These products experience a velocity component in the direction of wave propagation, as observed in numerical computations by Zhou et al. [10] and Gaillard et al. [9].

3.2. Phase-Averaged Fuel Injection Characteristics

A phase-averaged representation of the fuel jet development over a detonation period was used to characterize the statistically significant average fuel distribution in the channel. The method used to calculate the phase average is detailed in Appendix A. Phase-averaged vertical plane PLIF images from a single test at Case D operating conditions are presented in Fig. 6(a). A phase angle of $0°$ corresponds to the point in the cycle at which the detonation wave front (at $x=0$) is directly above the fuel injection site. Several features are recognizable in Fig. 6(a) that are comparable to Fig. 5. At low phase angles, pockets of high fuel concentration are observed more than $10\,\mu s$ after the detonation wave has passed a fuel injection site. After the detonation wave has passed, low fluorescence signal at the injector face indicates the stoppage of fuel injection into the combustor. As fresh fuel begins to enter the chamber, the jets are deflected in the $+y$ direction from $45°$ to $90°$, indicating contact with products of the previous detonation cycle.

The dots above several of the fuel jets in Fig. 6(a) indicate the estimated refill height for each jet. The method used for establishing the refill height based upon fluorescence intensity is detailed in Appendix B. The estimated refill heights diverge from the edge of the high-intensity jet structures, indicated by the curved dashed line, as the detonation cycle progresses. Given the strong negative relationship between acetone fluorescence

yield and temperature, discussed in Section 2.2, this suggests that acetone extinction may be taking place in a reaction zone between the measured refill height and the dashed line where reactants mix with high-temperature products from the previous cycle. Similar contact burning zones that grow in the x-direction throughout the cycle have been observed in numerical simulations [9, 10, 48]. Further observations and insights into this deflagrative contact zone burning behavior are provided in Section 3.3 with the OH* chemiluminescence measurements.

To further characterize the fuel mixing field, phase-averaged acetone-PLIF images for select horizontal planes (x = 3.2, 6.4, 9.5, and 12.7 mm) are presented in Fig. 6(b). The procedure for phase averaging was similar to the method applied in the vertical plane and is detailed in Appendix A. To highlight the fuel mixing characteristics, the intensity in each plane is scaled to the maximum intensity value in the plane. The maximum intensity was reduced by 80% from HP1 to HP3 and remained within a 10% range in planes HP3-HP4.

Near the injector, HP1 shows that the fuel is mostly concentrated near the center of the chamber throughout the detonation period. Moving away from the injector, the fuel streams become biased toward the side of the combustor from which they were injected (indicated by the white circles in Fig. 6(b)), a characteristic which is observed up through HP4 and continues throughout the detonation period. A consequence of this behavior is that there is a local deficiency of fuel on the opposite side (z-direction) from each fuel injector throughout the cycle, leading to a quasi-continuous sinusoidal-shaped fuel distribution most apparent in HP2–HP4 for $>210°$. This distribution indicates neighboring fuel streams (from opposite sides of the combustor) begin to cross the $z=0$ line at the jet extremities and mix together. Also, this fuel distribution appears to partly explain the fuel-deficient fuel jet cores that can be observed to
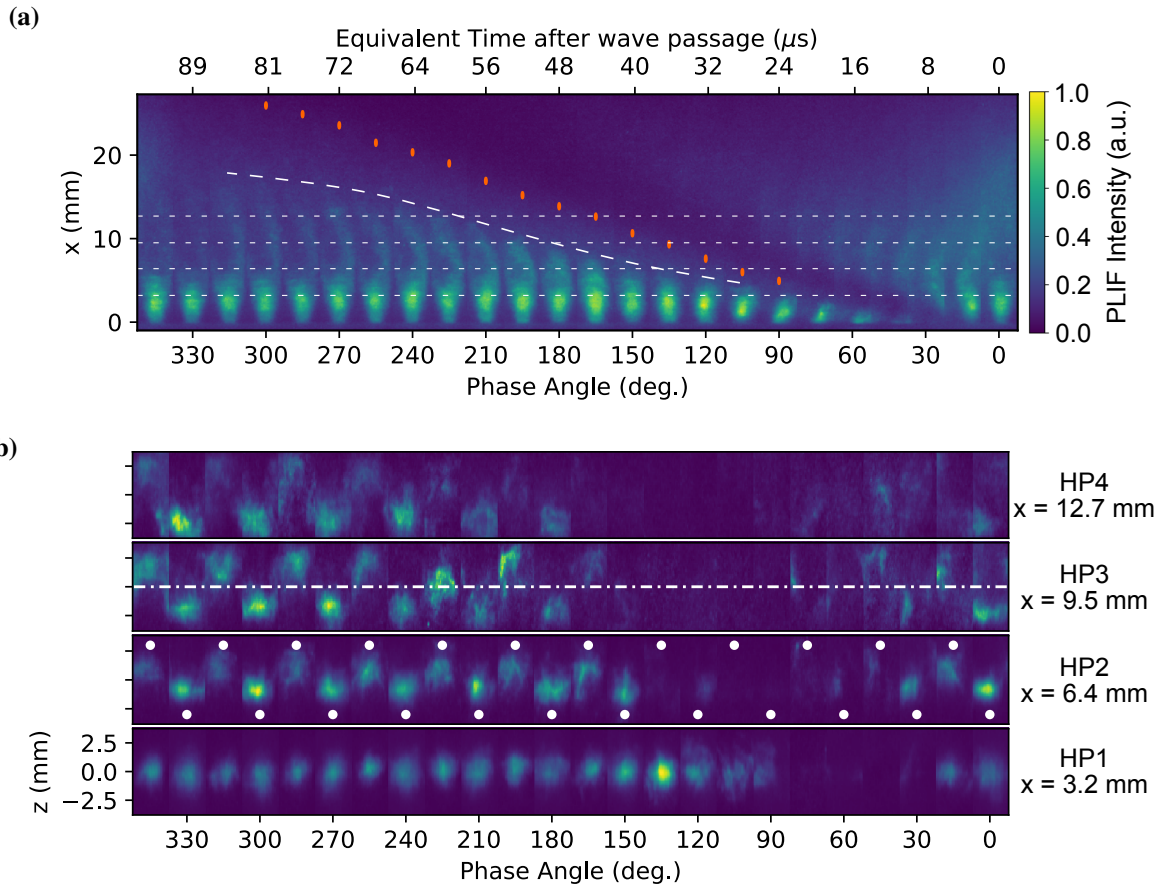
7

Figure 6: Phase-averaged PLIF images in the (a) vertical and (b) horizontal planes from tests at Case D operating conditions. Dots in (a) denote estimated refill height while the horizontal dashed lines in (a) correspond to HP1–4 locations from Fig. 2.

develop near 200° in Fig. 6(a) and that is highlighted at 61.62 ms in Fig. 5. Once the detonation wave passes, fuel continues to be observed more than 60° into the cycle in some planes, with a larger fraction of fuel remaining for a longer duration for HP4 compared to HP1, in agreement with Fig. 6(a). Another notable characteristic is the change to the fuel distribution before and after the detonation wave. After the detonation wave passes, the fuel becomes more well-distributed across the channel (z direction), which is most clearly seen in HP3 and HP4.

The three-dimensional phase-averaged acetone-PLIF fuel mixing field is revealed by stacking the horizontal planes from Fig. 6(b) in Fig. 7. Such reconstructions serve to illustrate the complex fuel injection and mixing field in the combustion chamber and also serve as a useful tool for qualitative evaluation of numerical models of such devices. It is clear from Fig. 7 that the detonation wave propagates through a highly stratified mixture of non-premixed reactants and products (shown later) and that this stratification evolves rapidly in space and time. It is expected that mixture stratification significantly affects detonation wave propagation in the channel, in part since detonation cell size variation is expected [49, 50]. Thus, the detonation wave characteristics are likely to significantly vary with increasing elevation above the injector face and this supposition is considered in the following section.
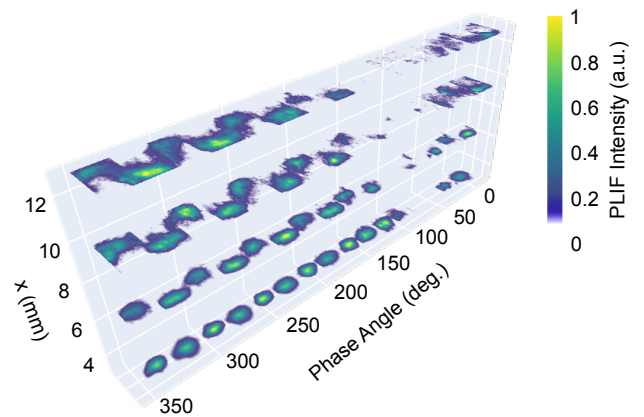

Figure 7: Three-dimensional overlay of phase-averaged PLIF images in the vertical (VP1) and horizontal planes (HP1–4) from tests at Case D operating conditions.

3.3. Acetone PLIF and OH* Chemiluminescence Imaging of Fuel Mixing and Detonation-Wave Dynamics

While spatially and temporally resolved imaging of the mixing field reveals combustor refill dynamics, the implications of these dynamics for detonation wave physics are of practical in-

8

terest. Well-informed injector designs can be guided by a more comprehensive understanding of the coupled behavior between the mixing field and detonation combustion. In an effort to relate the reactant mixing field to the resulting features of detonation wave propagation, this section presents simultaneous 100 kHz acetone PLIF and OH* chemiluminescence imaging, respectively. Acetone PLIF and OH* chemiluminescence images from the same time series as Fig. 5 are overlaid in Fig. 8. Estimations of the fuel refill height are denoted by green dots above each fuel injector as in Fig. 6(a). Since the PLIF FoV is approximately half of the height in the x-direction as the chemiluminescence FoV, fuel jet front locations outside of the PLIF FoV were extrapolated using the average jet velocity for the test and are shown instead by white dots. Jet fronts were also extrapolated inside the FoV when the refill height detection algorithm failed to make a reasonable measurement.

The chemiluminescence images in Fig. 8 reveal a forward-leaning detonation wave with a trailing heat release zone. The detonation wave front combustion intensity is relatively much lower near the injector face, coincident with the alternating pattern of high and low fuel concentrations at low x-values. This poorly-mixed injector nearfield is further corroborated by the observed fuel jet structures that remain behind the wave, indicating that pockets of high fuel concentration near the injector face are not fully consumed at the detonation front. Characteristics of an accompanying oblique shock above the detonation wave are also observed (denoted at 61.63 ms).

Another notable characteristic in Fig. 8 is a band of low heat release behind the detonation wave (outlined at 61.65 ms, between the white dashed lines). At the detonation front, this low heat release band is coincident with the top of the fuel refill height (note the fuel jet front projections from the PLIF, white

and green circles in Fig. 8) and the start of the oblique shock. Similar low intensity bands have been numerically predicted in non-premixed simulations [7, 9]. Gaillard, et al. attributed this phenomenon to a fuel-rich mixture with burnt gases in the refill zone, caused by a 4 μs delay between fuel and oxidizer injector recoveries. Similar differential injector recovery times resulting in fuel-rich or oxidizer-rich layers have been observed in other studies [23, 51–54].

These studies, in combination with the refill height measurements, suggest that a fuel-rich, noncombustible layer exists at the top of the refill zone, which is further supported by two additional observations. First, this low heat release layer becomes less pronounced for the leaner equivalence ratio cases (not shown). This is consistent with longer fuel injector recovery times, arising from lower fuel injection pressures than those seen in Case D, at which the equivalence ratio is elevated. Second, the fuel jet behavior about the $z=0$ plane from Fig. 6(b) indicates that as soon as the fuel jets recover, the fuel penetration depth across the channel (z-direction) is larger than later in the cycle, indicating there is a longer delay in the recovery of the oxidizer flow. This point is quantified by measurements of the z-location of the intensity-weighted centroids ($\bar{z}$) of the phase-averaged jet images from Fig. 6(b). These measurements are provided in Fig. 9 where positive values of $\bar{z}$ indicate that the jet has shifted toward the side of the chamber from which it was injected. The curves represent a 3-point moving average of the data. While the jets in planes HP1 and HP2 are relatively stable after 150°, the data in planes HP3 and HP4 displays unsteady behavior and a continued shift toward higher $\bar{z}$ values until the 250° mark. This is particularly clear from the images in HP3 in Fig. 6(b). Thus, the flow field appears unsteady for a time after initial fuel recovery, suggesting that there is a delay
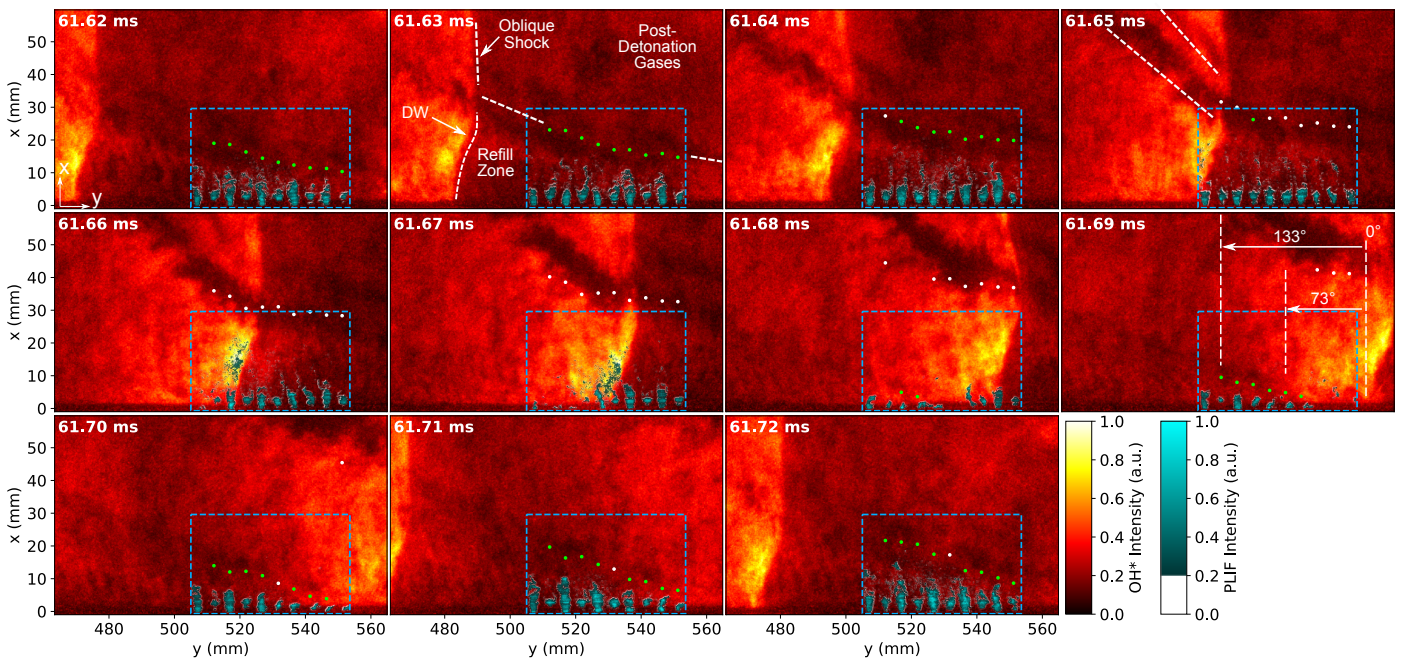

Figure 8: Simultaneous OH* chemiluminescence and acetone-PLIF images for a single detonation cycle from a test at Case D operating conditions. Note that this time sequence (and PLIF data) corresponds to Fig. 5. DW - detonation wave, FoV - field of view.
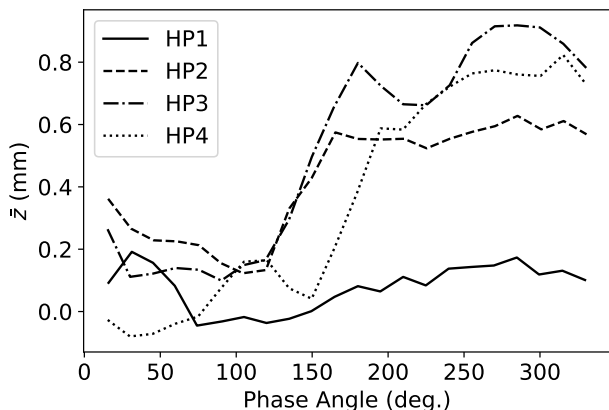
9

Figure 9: Intensity-weighted jet centroid positions in the *z*-axis as a function of phase angle for planes HP1–4 at Case D operating conditions. A positive $\bar{z}$ value indicates that the jet has moved to the side of the chamber from which it was injected.

in the oxidizer recovery compared to the fuel recovery. While jets in crossflow have been shown under some conditions to exhibit temporary increases in penetration, the suspected unsteadiness in the oxidizer stream would have a significant impact on the fuel jet trajectory, especially moving up the channel (x-direction) [55].

The phase-averaged OH* chemiluminescence and acetone-PLIF for Case D is shown in Fig. 10. Similar characteristics are observed in the phase-averaged field as were also observed in the instantaneous fields in Fig. 8. The wave displays a forward lean, an oblique shock, and unburned fuel remaining behind the detonation wave that is more pronounced near the injector. Jet front location measurements reveal a linear fuel refill height and extrapolations show average fuel refill heights at the wave of 31 mm. The phase-averaged refill height projections confirm that the fresh fuel supply at the top of the fuel refill intersects the detonation wave at the upper x-boundary of the non-reacting band that continues behind the detonation wave. This result further supports the hypothesis that this band of low heat release

is a fuel-rich and non-reacting zone.

A major characteristic observed in both Fig. 8 and Fig. 10 is the presence of heat release not only at the detonation front, but throughout the flowfield. In particular, heat release is observed behind the detonation wave, throughout the post-detonation wave gases, and throughout the reactant refill zone. This is now considered in more detail in relation to the measured fuel mixing field. Figure 11 presents the phase-averaged chemiluminescence image from 100–300°, extracted from Fig. 10. At high x-values away from the injector (Zone 1), Fig. 11(a) depicts a diffuse region of heat release well above the reactant refill height and thus occupied by gases from the previous cycle. Below Zone 1, alternating bands of high and low chemiluminescence are observed, and highlighted further in Fig. 11(c), which gives the intensity profile in the x-direction at 200°. The measured fuel refill height, as indicated by the fuel jet front locations (green dots), in Fig. 11 indicate that the fuel jet fronts lie in Zone 3, coinciding with a local increase in the heat release (relative to Zones 2 and 4). Since this region is near the top of the fuel refill and, thus, should be in close proximity to high-temperature products of the previous cycle, the Zone 3 heat release is not unexpected if there is any remaining oxidizer in the channel to react with.

While the cause of the lower-luminosity area above the fuel refill height, Zone 2, is more difficult to ascertain based on the measured data, it is still instructive to postulate on the origin of this region. Zone 2 is above the measured fuel refill height (Zone 3) and below the evident products of the previous cycle (Zone 1). One possibility is that Zone 2 consists of product gases that have cooled down in the wake of the detonation wave. Another possibility is that Zone 2 is also fuel rich, with an altered thermodynamic state (e.g. preheated or vitiated). As the fuel jets first turn back on after the detonation wave, the fuel first issued into the channel is in contact with the high-temperature products of the previous cycle. Significant mixing between the fuel and the hot products would elevate the fuel temperature causing pyrolysis of the acetone tracer, which would be reflected as near-zero PLIF signal. This would cause
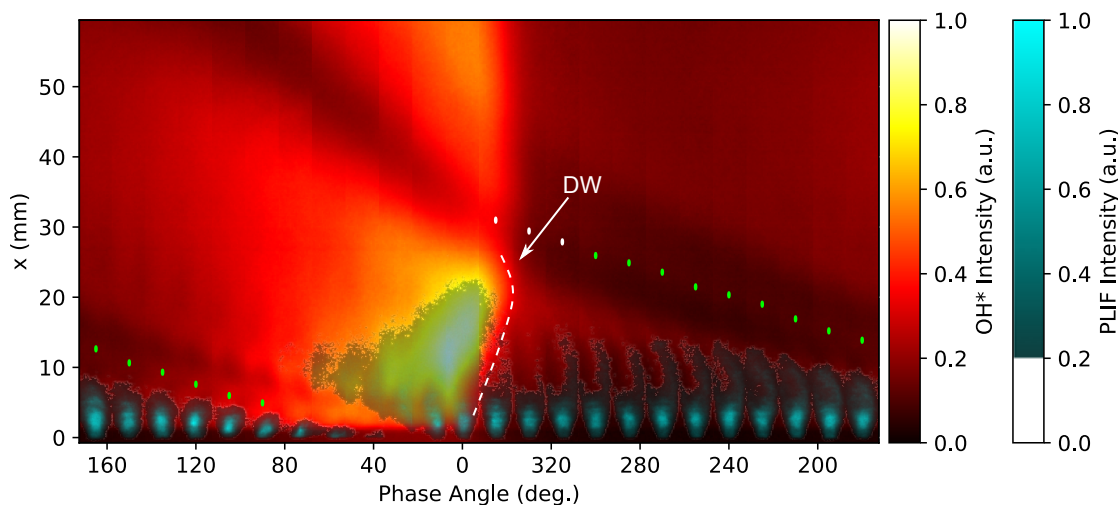

Figure 10: Overlaid phase-averaged acetone-PLIF and OH* chemiluminescence images from a test at Case D operating conditions. DW - detonation wave.
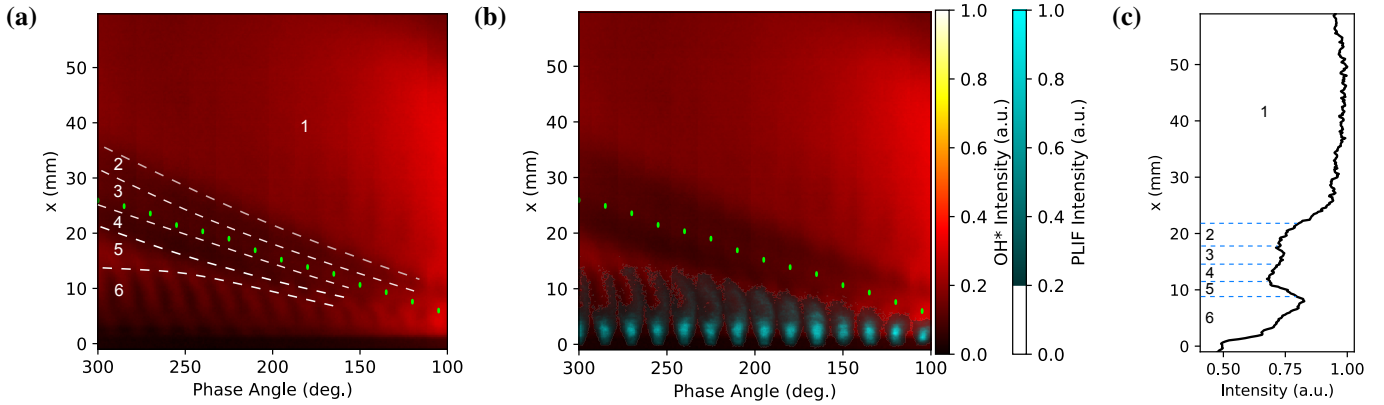
10

Figure 11: Phase-averaged chemiluminescence images for Case D extracted from Fig. 10 and shown (a) without and (b) with overlaid phase-averaged PLIF images, and (c) column-wise OH* intensity profile at 200°.

the refill height estimates to fall below the true values. However, this seems like an unlikely possibility as the acetone-PLIF is able to register fuel very near the injector face and also track the temporal refill history. Another possibility is that Zone 2 is comprised of unburned reactants from the previous detonation cycle that either consist of mostly oxidizer or whose temperature or vitiation level have increased, causing acetone pyrolysis. This agrees with the fuel stratification and poor mixing at the base of the detonation wave, to which Zone 2 can be traced.

The difference in fuel and oxidizer recovery times, suggested in Fig. 8 and Fig. 10, indicates that Zone 4 may be a non-reacting, fuel-rich region, introduced before the oxidizer injector significantly recovers. This is opposed to the fuel in the contact zone (Zone 3), which is able to mix with remaining oxygen from the previous cycle. Though a local increase in PLIF signal might be expected in Zone 4, examination of initial fuel recovery from 40°–160° in Fig. 10 indicates that the fuel which eventually forms Zone 4 has been exposed to high-temperature gases, as evident from the prevalence of OH* signal at the top of the fuel refill zone during this part of the cycle. As a result, the acetone fluorescence yield is diminished and fuel presence in Zone 4 is marked only by the diffuse fluorescence signal observed in Fig. 6(a), as discussed in Section 3.2. Another band of heat release, labeled Zone 5, lies at the downstream edge of the high-intensity acetone fluorescence signals and expands in the x-direction from phase angles of 250-300°. Burning in Zone 5 indicates that the oxidizer injector has recovered and created a second contact burning zone. While fuel is observed all the way up to the refill height (as indicated by the green dots in Fig. 10), the expanding zone of low fluorescence observed beneath the refill height in Fig. 6 further corroborates some amount of heat release occuring. A similar experimental observation of two contact burning zones has been documented in [23, 51]. The mixture of fuel and oxidizer in Zone 5 may be ignited by recirculating products near the chamber walls that could not be expelled by the fuel streams alone. As the oxidizer supply pushes these recirculated products downstream, new reactants are not exposed to such high temperatures, resulting in a region of lower OH* signal in Zone 6.

In Zone 6, heat release is observed all around each fuel injection location above x=5 mm. Figure 11(b) confirms that these zones of heat release correspond to the regions of the fuel jets where PLIF signal is lost. While the chemiluminescence images are path-averaged, this observation indicates that the lack of fluorescence in these areas may be caused not only by fuel flow in the z-direction, but also by acetone oxidation or pyrolysis (by way of burning or mixing with hot products). These localized heat release zones in the refill region create temperature field stratification in addition to the aforementioned mixture composition stratification. Also note that the fuel jets exhibit a -y lean moving up the channel, most apparent by noting the chemiluminescence distribution at each injector location in Fig. 11(a).

Figure 12 illustrates the flow field in the chamber for Case D operating conditions in a simplified manner, as informed by the fuel distribution from acetone PLIF and heat release as indicated by OH* chemiluminescence images. The detonation wave presents a forward lean and weakened heat release near the injector face. The oblique shock and detonation wave are separated by a non-reacting zone, likely occupied by a fuel-rich mixture of partially pyrolyzed fuel and recirculated combustion products. After the detonation wave passes a fuel injection site, fuel and oxidizer injection are temporarily halted as the pressure behind the detonation wave overcomes the manifold pressures. A volume of high fuel concentration detaches from the injector plate and survives the detonation front before being burned in the wake of the detonation wave. After a recovery period, fuel injection resumes slightly before oxidizer injection. This produces the fuel-rich layer that contributes to the non-reacting zone above the detonation front. The fuel introduced before oxidizer recovery is also injected into the high-temperature gases in the wake of the detonation wave, causing heating and partial pyrolysis of the fuel (and acetone). Oxidizer flow is then reestablished and the reactants begin to mix. Deflagration reactions begin near the center plane of the channel where fuel and oxidizer mixing is most intense. These reactions consume the central part of the fuel jets along the laser plane, leading to the appearance of hollow fuel jets in Fig. 5. The
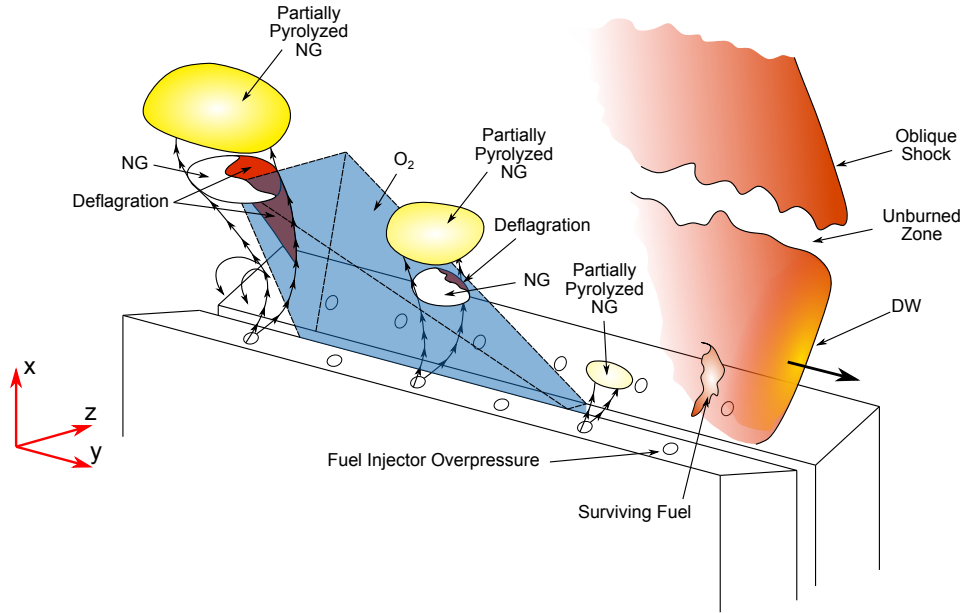
11

Figure 12: Schematic representation of the flow environment in the chamber. Features not drawn to scale. NG - Natural Gas, DW - Detonation Wave.

expanding oxidizer stream then forces the fuel jets back toward the side of the channel from which they were introduced as the deflagration reaction front expands. Eventually, another detonation wave arrives to propagate through the stratified reactant field and to begin the cycle again.

3.4. Quantification of Fuel Injection Recovery Times and Jet Velocities

While qualitative evaluations of combustor physics serve to uncover significant phenomena and to highlight trends for further study, quantitative measurements such as injector recovery times and reactant flow velocities have significant implications for design features such as the detonation wave height and combustor length. Since there are few experimental observations of injector recovery time currently available in the RDE literature [24], this section provides additional measurements of injector recovery times and fuel jet velocities in an operating detonation combustor.

Two methodologies were implemented for calculating the fuel jet recovery times. The first methodology relies on analysis of the instantaneous and simultaneous acetone PLIF and OH* chemiluminescence images and is described first. For Cases A, C, and D, fuel injector recovery times in the vertical plane PLIF images were studied to characterize the injector response at different equivalence ratios. For a single jet, the spatial average of a 20x20 pixel region near the injection surface, highlighted in Fig. 13(a), was monitored in time. This area was centered in the +y half of the image since the fuel jets were seen to favor that direction during initial recovery, as explained in the discussions of Fig. 5 and Fig. 6. A representative intensity profile from this region over one detonation cycle for a jet at Case D operating conditions is presented in Fig. 13(b). In this case, the detonation wave is located at the injection location at t=0 sec, as determined from the simultaneous OH* chemiluminescence images. In practice, the wave arrival time at a particular injector often occurred in between frames. In this case, the time of wave arrival and the intensity at that point were interpolated using the wave location data from the OH* chemiluminescence images. Each cycle is marked by a sharp drop in signal intensity, denoting the passage of a detonation wave and the cessation of fuel injection. Following the cycle low point, a 10% recovery of the signal lost from the intensity value at a 0° phase angle was chosen to constitute a sign of jet recovery. The time at which the intensity level reached 10% recovery was estimated using interpolation, as shown in Fig. 13(b). The time between the wave arrival and initial recovery, highlighted by the shaded region, was measured for each cycle at each fuel injection site. The number of samples collected were 65, 94, and 106 for single tests at Case A, C, and D operating conditions, respectively. The higher number of samples for the tests at Case C and D operating conditions is attributable to the increased cycle frequency, which resulted in a greater number of observed detonation cycles for the same laser burst width.

Table 2 provides the average fuel jet recovery times for single tests, $\bar{\Delta}_{rec}$, the standard deviations (σ) of $\bar{\Delta}_{rec}$, and also the recovery times calculated as a percentage of the cycle period, $\%\bar{\Delta}_{rec}$ (= $100\bar{\Delta}_{rec}f$). The fuel recovery time falls 43% as the equivalence ratio increases from 0.83 to 1.26. At the same time, the average fuel manifold pressure, $\bar{P}_{FM}$, increases 42%, indicating that the fuel manifold pressure plays a dominant role in determining the recovery time. It is interesting to note that the recovery times observed at Case C operating conditions are comparable with the only prior experimental measurements of fuel recovery time in an RDE: Rankin et al. reported fuel recovery times of 18–22% of the cycle period in a H_2-air RDE at a stoichiometric condition [24]. However, their measurements were made by comparing instantaneous images captured during different cycles since their measurement rate could not resolve
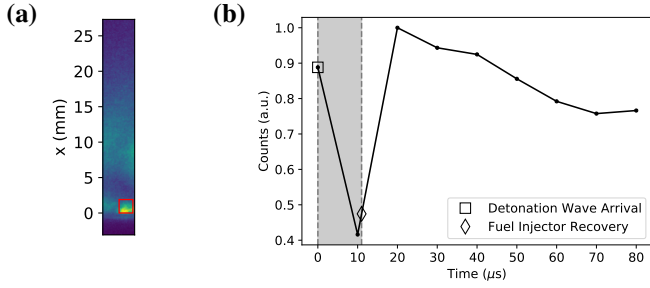
12

any single detonation cycle.

Figure 13: (a) Fuel jet image highlighting the region used in injection recovery time analysis and (b) average cycle intensity profile of PLIF signal from the region shown in (a) for a test at Case D operating conditions.

The second methodology for calculating the fuel jet recovery time relies on analysis of the phase-averaged acetone PLIF and OH* chemiluminescence images and is now described. Performing a recovery time analysis on a phase-averaged image series, like the one shown in Fig. 6(a), affords greater temporal resolution of the recovery process. At each operating condition, jet images from a single test were phase-averaged using 50 phase bins to divide the cycle. A similar recovery time analysis was then performed on the phase-averaged images as was applied to the instantaneous images. Figure 14 presents the intensity profiles of the region of interest (from Fig. 13(a)) for Case A and Case D operating conditions. A $+/-1\sigma$ intensity range, denoted by the shaded region, was calculated for each phase bin based upon the intensity variation of the images being averaged. A phase angle of $0°$ corresponds to the point in time at which the $x=0$ wave position is at the injector centerline. For each case, a centered three-point moving average through the data was used for recovery time calculations, displayed as a dashed line through the data. Again, a 10% recovery of the intensity drop from $0°$ phase angle to the cycle minimum constituted injector recovery. The average number of frames sampled in each phase bin for Cases A, C, and D were 18, 18, and 20, respectively. The phase-averaged recovery times, Δ_{rec}^{pa}, are presented in Table 2. The instantaneous measurements differ from the phase-averaged results by less than 3 μs in all cases, indicating that the average instantaneous measurements provide an accurate evaluation of the recovery time.

Average fuel jet velocities (x-direction), $\bar{V}$, calculated from the progression of measured fuel jet front locations, are also presented in Table 2 with standard deviations. Figure 15(a) reveals an approximately normal distribution of velocity measurements about the mean for a single test at Case D operating conditions. The mean value is denoted by the vertical dashed line and a normal probability distribution function is plotted alongside the raw data. Figure 15(b) plots all velocity measurements for the same test as a function of measurement position above the injector face. Due to the high measurement variance, no conclusions can be drawn concerning the possibility of jet acceleration in the x-direction. Similarly, comparisons of velocity measurements at different fuel injection locations showed no statistically significant variations.
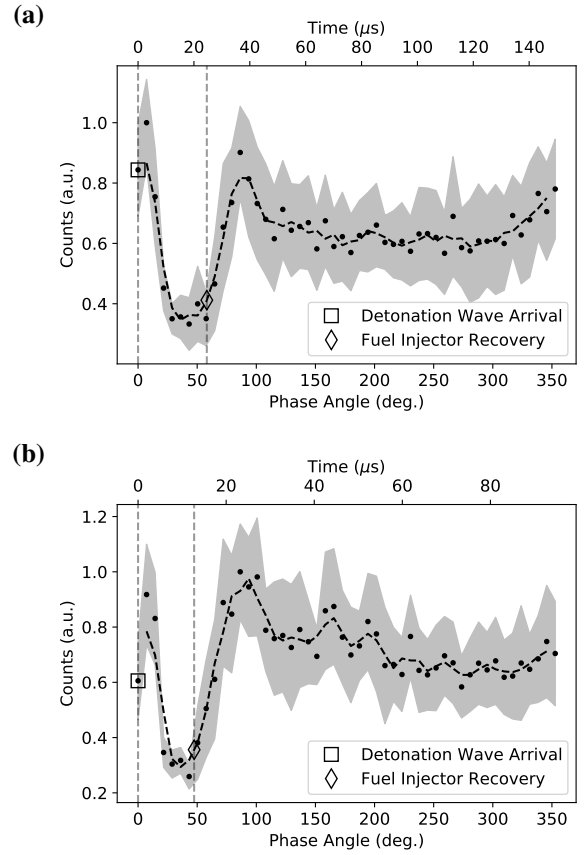

Figure 14: Phase-averaged intensity profiles of the spatial region highlighted in Fig. 13(a) for single tests at (a) Case A and (b) Case D operating conditions.

Phase-averaged fuel jet front tracking results are plotted in Fig. 16. The data show a linear progression for all test cases with nearly equal slopes, as reflected in the close agreement between phase-averaged fuel jet velocity measurements, V^{pa} (i.e. slope of the linear fit), given in Table 2. These velocities lie within a quarter of a standard deviation of the average instantaneous velocities. In both the instantaneous and phase-averaged velocity measurements, the close agreement between the test cases, despite the changes in fuel manifold pressure, indicates that the fuel orifices are sonic according to their design and that the refill height should be mainly determined by recovery time and the detonation cycle frequency.

Table 2: Equivalence ratio, detonation cycle frequency, average fuel manifold pressure, average instantaneous and phase-averaged fuel injector recovery times in μs and as a percentage of the cycle period, and average instantaneous and phase-averaged fuel jet velocities for Cases A, C, and D.

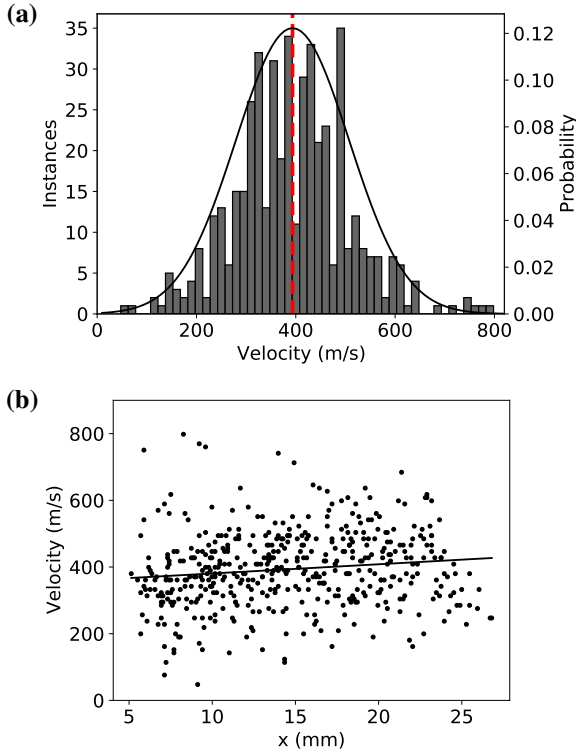| Case	ϕ	f (kHz)	$\bar{P}_{FM}$ (kPa)	$\bar{\Delta}_{rec}/\sigma$ (μs)	$\%\bar{\Delta}_{rec}$	Δ_{rec}^{pa} (μs)	$\%\Delta_{rec}^{pa}$	$\bar{V}/\sigma$ (m/s)	V^{pa} (m/s)
A	0.83	6.6	393	23.8/5.0	15.8	24.6	16.2	412/155	374
C	0.97	10.6	455	17.6/2.9	18.7	15.0	16.1	416/141	372
D	1.26	10.6	558	13.7/2.9	14.4	12.7	13.2	393/114	386

(a)

(b)

Figure 15: (a) Histogram of velocity measurements with a normal probability density function plotted alongside and (b) velocity as a function of x-position with a linear least-squares fit for a test at Case D operating conditions.
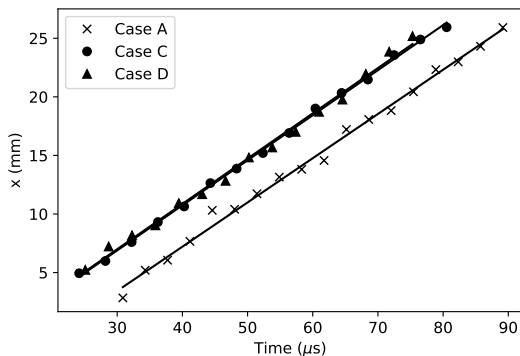

Figure 16: Phase-averaged jet front positions in time for single tests at Case A, C, and D operating conditions.

4. Conclusions

Fuel injection and reactant mixing in a linear detonation combustor have here been spatially and temporally resolved with 100 kHz acetone PLIF measurements, while combustion processes were simultaneously captured using 100 kHz OH* chemiluminescence imaging. The simultaneous measurements enabled detailed characterization of key processes within detonative combustors, as summarized below.

- *Fuel injector recovery time:* Following passage of a detonation wave, the inflow of freshly injected fuel is temporarily halted. This work demonstrated methods for measuring the instantaneous and phase-averaged fuel injector recovery time, defined as the time between the instant of detonation arrival and the point when the fuel injector again begins to issue fresh fuel into the detonation channel. This is an important parameter for establishing the correct boundary conditions for numerical simulations. The measured fuel injector recovery times varied from 14.4%–18.7% of the detonation cycle period as a function of the detonation cycle frequency and fuel manifold pressure.

- *Deflagrative burning before the detonation wave:* The OH* images indicated that there was heat release throughout the channel ahead of the detonation wave. By resolving the reactant refill process, it was further observed that this heat release is present in both the post-detonation products from the prior cycle as well as in the reactant refill zone, with sufficient unburned fuel and oxygen present in these zones to support the continued propagation of the detonation wave. Additional measurements are needed to quantify the fraction of fuel consumed in this deflagrative mode.

- *Unburned fuel behind the detonation wave:* From the acetone PLIF images, fuel was observed up to $60°$ (17% of the detonation period) after the detonation wave had passed, signifying that the detonation wave did not consume all of the fuel. The ultimate elimination of acetone fluorescence signal and the persistence of OH* well behind the detonation wave indicate that the fuel ultimately mixes with the high-temperature detonation products and that deflagrative combustion occurs over a spatially-broad region behind the detonation wave.

- *Unburned fuel layer at the leading edge of the reactant refill:* A mismatch in the fuel and oxidizer injector recovery time was identified using overlaid images of the fuel distribution and heat release fields. The mismatch resulted

14

in multiple contact burning zones as well as a region of low heat release at the tip of the fuel jets. The contents of this region exited the chamber as unburned reactants, providing experimental confirmation of fuel and oxidizer injector recovery time mismatch as a source of combustion inefficiency.

- *Detonation wave-front structure:* The combustion intensity of the detonation wave was reduced near the injector face, where the PLIF images indicate jets of high fuel concentration that are not yet well mixed with the oxidizer. This mixture stratification results in low heat release at the base of the detonation wave. Moreover, the improved mixing further away from the injector, in combination with the partial vitiation (as indicated from the OH* images) may explain why the upper portion of the detonation wave front leans forward. Overall, shorter fuel injector recovery times were associated with higher detonation cycle frequencies, shorter fuel refill heights, and more compact detonation waves.

These results illustrate the ability of simultaneous 100 kHz acetone PLIF and OH* chemiluminescence to improve the fundamental understanding of RDE operation and provide data for more thorough evaluation of numerical simulations. The detailed information afforded by this approach provides new insight into RDE processes that affect combustion and thermodynamic inefficiencies.

Acknowledgments

Appendix A. Calculation of Phase-Averaged Images

Acetone-PLIF phase averaging was accomplished by first dividing the FoV into images of the individual fuel jets. To calculate the phase position of a fuel jet image, the points in time at which detonation waves reached that injector were considered. Every point in time at which a detonation wave reached a given fuel injector was determined by extracting wave positions at the injector face from simultaneous OH* chemiluminescence images. The positions were measured using the same edge detection algorithm used for Fig. 4. When wave positions on either side of an injector were recorded in sequential frames, the time at which the wave reached the injector was estimated using linear interpolation and assuming a constant wave speed. The wave speed was calculated as the average velocity of the measured wave fronts over a 15 ms time interval, which

was centered on the PLIF collection period. Once the temporal positions of wave arrivals were established at a given fuel injection location, the phase position of that injector at every frame between wave arrivals could be calculated. Phase bins were established depending on the required resolution and the jet images were sorted into the bins for averaging, regardless of injection location in the chamber.

In Fig. 6(a), the phase-averaged representation of every fuel jet was calculated using 38 instantaneous images. The phase separation between neighboring phase bins was chosen to equal the average phase difference of neighboring jets in the experiment. Horizontal plane images in Fig. 6(b) were phase-averaged in the same manner as the vertical plane images with the exception that jets from fuel injection sites on opposing sides of the oxidizer injector were averaged separately. This, in addition to a smaller field of view, reduced the number of instantaneous images in each phase bin relative to the vertical plane measurements. Each phase-averaged fuel jet image in the horizontal planes was created using 8.3 instantaneous images on average.

Chemiluminescence images were phase averaged in the same manner as the vertical plane PLIF images. Each instantaneous image was divided into subimages centered on fuel injection locations with widths equal to the injector spacing. As illustrated at 61.59 ms in Fig. 8, the phase position of each fuel injection location (and therefore subimage) was determined in the same manner as for the vertical plane PLIF images. Subimages were grouped by phase position and averaged irrespective of their original position in the FoV. Stacking sequential phase averaged subimages horizontally renders a phase-averaged image of the full cycle. This method was chosen to increase the sample size of each phase bin and to offer a full view of the detonation cycle. Chemiluminescence frames obtained over a 15 ms time interval were phase-averaged to create the image in Fig. 10.

Appendix B. Refill Height Measurement Method

Refill heights were estimated by processing the row-averaged intensity profile of each fuel jet in the *x*-direction and identifying the *x*-location where the profile decayed to the background level, as shown in Fig. B.17(a). The background level for each jet was determined by first dividing each jet image into 16 vertically stacked bins of 20 pixel rows each. As illustrated in Fig. B.17(b), the spatially averaged intensity of each bin was monitored in time and the minimum intensity levels that these signals reached during each detonation cycle were recorded. For each bin, the average of the minimum cycle intensity values was taken to be the background intensity level of the bin. The background levels were then subtracted from the corresponding bins for every frame, producing the background subtracted profile in Fig. B.17(a). A moving average of the background-subtracted intensity profile was then used to smooth the signal. The jet front was declared at the point where the moving average fell below 500 counts (0.8% saturation). This threshold was set according to observed cycle-to-cycle variation in the background value.
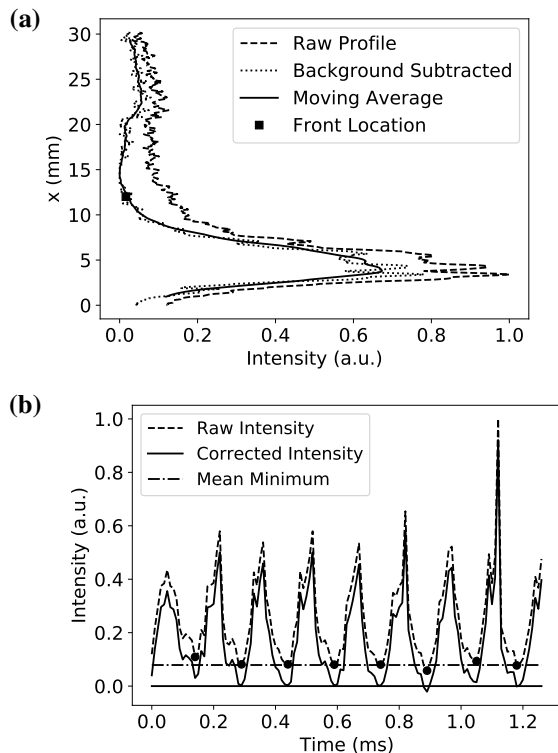
15

(a)

(b)

Figure B.17: (a) Row-averaged intensity profiles of a single jet before and after background subtraction used to determine the jet front location. (b) Temporal profile of a single spatially averaged bin, illustrating the mean background subtraction process.

References

[1] D. Kellari, What's next for the airliner? historical analysis and future predictions of aircraft architecture and performance, Master's Thesis, Massachussets Institue of Technology, Cambridge, MA.

[2] P. Sutton, George, O. Biblarz, Rocket Propulsion Elements, John Wiley & Sons, 2001.

[3] P. Wolanski, Application of the continuous rotating detonation to gas turbine, Appl. Mech. Mater. 782 (2015) 3–12. doi:10.4028/www.scientific.net/AMM.782.3.

[4] E. Wintenberger, J. E. Shepherd, Model for the performance of air-breathing pulse-detonation engines, J. Propul. Power 22 (2006) 835–844. doi:10.2514/1.5792.

[5] I. Q. Andrus, M. D. Polanka, P. I. King, F. R. Schauer, J. L. Hoke, Experimentation of premixed rotating detonation engine using variable slot feed plenum, J. Propul. Power 33 (6) (2017) 1448–1458. doi:10.2514/1.B36261.

[6] J. Fujii, Y. Kumazawa, A. Matsuo, S. Nakagami, K. Matsuoka, J. Kasahara, Numerical investigation on detonation velocity in rotating detonation engine chamber, Proc. Combust. Inst. 36 (2017) 2665–2672. doi:10.2514/1.A34763.

[7] J. Sun, J. Zhou, S. Liu, Z. Lin, Numerical investigation of a rotating detonation engine under premixed/non-premixed conditions, Acta Astronaut. 152 (2018) 630–638. doi:10.1016/j.actaastro.2018.09.012.

[8] D. A. Schwer, K. Kailasanath, Physics of heat-release in rotating detonation engines, 53rd AIAA Aerospace Sciences Meeting, AIAA 2015-1602, 2015. doi:10.2514/6.2015-1602.

[9] T. Gaillard, D. Davidenko, F. Dupoirieux, Numerical simulation of a rotating detonation with a realistic injector designed for separate supply of gaseous hydrogen and oxygen, Acta Astronaut. 141 (2017) 64–78. doi:10.1016/j.actaastro.2017.09.011.

[10] R. Zhou, J. P. Wang, Numerical investigation of flow particle paths and thermodynamic performance of continuously rotating detonation engines, Combust. Flame 159 (2012) 3632–3645. doi:10.1016/j.combustflame.2012.07.007.

[11] C. A. Nordeen, D. Schwer, F. Schauer, J. Hoke, T. Barber, B. M. Cetegen, Role of inlet reactant mixedness on the thermodynamic performance of a rotating detonation engine, Shock Waves 26 (2016) 417–428. doi:10.1007/s00193-015-0570-7.

[12] R. Zhou, J. P. Wang, Numerical investigation of shock wave reflections near the head ends of rotating detonation engines, Shock Waves 23 (2013) 461–472. doi:10.1007/s00193-013-0440-0.

[13] X. Y. Liu, M. Y. Luan, Y. L. Chen, J. P. Wang, Flow-field analysis and pressure gain estimation of a rotating detonation engine with banded distribution of reactants, Int. J. Hydrogen Energy 45 (2020) 19976–19988. doi:10.1016/j.ijhydene.2020.05.102.

[14] V. Athmanathan, J. Braun, Z. Ayers, J. Fisher, C. Fugger, S. Roy, G. Paniagua, T. Meyer, Detonation structure evolution in an optically-accessible non-premixed H_2-air RDC using MHz rate imaging, AIAA SciTech Forum, AIAA 2020-1178, 2020. doi:10.2514/6.2020-1178.

[15] B. A. Rankin, D. R. Richardson, A. W. Caswell, A. Naples, J. L. Hoke, F. R. Schauer, Chemiluminescence imaging of an optically accessible non-premixed rotating detonation engine, Combust. Flame 176 (2017) 12–22. doi:10.1016/j.combustflame.2016.09.020.

[16] R. M. Gejji, T. Buschhagen, C. D. Slabaugh, Occurrence of rotating detonation waves in a jet-stabilized combustor with premixed injection, J. Propul. Power 37 (4) (2021) 1–5. doi:10.2514/1.B38292.

[17] D. P. Stechmann, S. Sardeshmukh, S. D. Heister, K. Mikoshiba, Role of ignition delay in rotating detonation engine performance and operability, J. Propul. Power 35 (1) (2018) 125–140. doi:10.2514/1.B37117.

[18] C. A. Fugger, J. G. Lopez, K. D. Rein, S. Roy, A. W. Caswell, The dynamics of a non-premixed rotating detonation engine from time-resolved temperature measurements, Proc. Combust. Inst. 38 (2021) 3787–3795. doi:10.1016/j.proci.2020.06.373.

[19] J. Kindracki, A. Kobiera, P. Wolański, Z. Gut, M. Folusiak, K. Swiderski, Exprimental and numerical study of the rotating detonation engine in hydrogen-air mixtures, Prog. Propul. Phys. 2 (2012) 555–582. doi:10.1051/eucass/201102555.

[20] V. Anand, A. St. George, R. Driscoll, G. E, Characterization of instabilities in a rotating detonation combustor, Int. J. Hydrogen Energy 40 (2015) 16649–16659. doi:10.1016/j.ijhydene.2015.09.046.

[21] F. A. Bykovskii, E. F. Vedernikov, Continuous detonation of a subsonic flow of a propellant, Combust., Explos. Shock Waves (Engl. Transl.) 39 (2003) 323–334. doi:10.1023/A:1023800521344.

[22] B. R. Bigler, J. W. Bennewitz, S. A. Danczyk, W. A. Hargus, Rotating detonation rocket engine operability under varied pressure drop injection, J. Spacecr. Rockets 58. doi:10.2514/1.A34763.

[23] T. Sato, F. Chacon, L. White, V. Raman, M. Gamba, Mixing and detonation structure in a rotating detonation engine with an axial air inlet, Proc. Combust. Inst.doi:10.1016/j.proci.2020.06.283.

[24] B. A. Rankin, C. A. Fugger, D. R. Richardson, K. Y. Cho, J. L. Hoke, A. W. Caswell, J. R. Gord, F. R. Schauer, Evaluation of mixing processes in a non-premixed rotating detonation engine using acetone PLIF imaging, 54th AIAA Aerospace Sciences Meeting, AIAA 2016-1198, 2016. doi:10.2514/6.2016-1198.

[25] B. A. Rankin, J. R. Cordoni, K. Y. Cho, J. L. Hoke, F. R. Schauer, Investigation of the structure of detonation waves in a non-premixed hydrogen–air rotating detonation engine using mid-infrared imaging, Proc. Combust. Inst. 37 (2019) 3479–3486. doi:10.1016/j.proci.2018.09.036.

[26] K. Schwinn, R. Gejji, B. Kan, S. Sardeshmukh, S. Heister, C. D. Slabaugh, Self-sustained, high-frequency detonation wave generation in a semi-bounded channel, Combust. Flame 193 (2018) 384–396. doi:10.1016/j.combustflame.2018.03.022.

[27] R. YoKoo, K. Goto, J. Kasahara, V. Athmanathan, J. Braun, G. Paniagua, T. Meyer, A. Kawasaki, K. Matsuoka, A. Matsuo, I. Funaki, Experimental study of internal flow structures in cylindrical rotating detonation engines, Proc. Combust. Inst.doi:10.1016/j.proci.2020.08.001.

[28] I. V. Walters, R. M. Gejji, S. D. Heister, C. D. Slabaugh, Flow and performance analysis of a natural gas-air rotating detonation engine with high-speed velocimetry, Combust. Flame 232 (2021) 111549. doi:10.1016/j.combustflame.2021.111549.

[29] S. Prakash, R. Fievet, V. Raman, J. Burr, K. Yu, Analysis of the detonation wave structure in a linearized rotating detonation engine, AIAA J. 58 (2020) 5063–5077. doi:10.2514/1.J058156.

[30] T. C. Rathsack, J. R. Burr, B. R. Bigler, J. W. Bennewitz, Analysis of single wave behavior in a linear detonation channel using injector plane oriented direct imaging, AIAA Scitech Forum, AIAA 2021-1380, 2021. doi:10.2514/6.2021-1380.

[31] J. Sosa, K. A. Ahmed, R. Fievisohn, J. Hoke, T. Ombrello, F. Schauer, Supersonic driven detonation dynamics for rotating detonation engines, Int. J. Hydrogen Energy 44 (2019) 7596–7606. doi:10.1016/j.ijhydene.2019.02.019.

[32] C. Bedick, D. Ferguson, P. Strakey, Characterization of rotating detonation engine injector response using laser-induced fluorescence, J. Propul. Power 35 (4) (2019) 827–838. doi:10.2514/1.B37309.

[33] J. Duvall, M. Gamba, Characterization of reactant mixing in a rotating detonation engine using schlieren imaging and planar laser induced fluorescence, AIAA Joint Propulsion Conference, AIAA 2018-4690, 2018. doi:10.2514/6.2018-4690.

[34] R. Bluemner, M. D. Bohon, C. O. Paschereit, E. J. Gutmark, Experimental study of reactant mixing in model rotating detonation combustor geometries, Flow, Turbul. Combust. 102 (2018) 255–277. doi:10.1007/S10494-018-9966-7.

[35] Z. M. Ayers, A. I. Lemcherfi, E. W. Plaehn, C. D. Slabaugh, T. R. Meyer, C. A. Fugger, S. Roy, Application of 100 kHz acetone-plif for the investigation of mixing dynamics in a self-excited linear detonation channel, AIAA SciTech Forum, AIAA 2021-0554, 2021. doi:10.2514/6.2021-0554.

[36] M. C. Thurber, F. Grisch, R. K. Hanson, Temperature imaging with single- and dual-wavelength acetone planar laser-induced fluorescence, Opt. Lett. 22 (1997) 251–253. doi:10.1364/OL.22.000251.

[37] S. P. Kearney, F. V. Reyes, Quantitative temperature imaging in gas-phase turbulent thermal convection by laser-induced fluorescence of acetone, Exp. Fluids 34 (2003) 87–97. doi:10.1007/s00348-002-0537-1.

[38] T. R. Meyer, J. C. Dutton, R. P. Lucht, Vortex interaction and mixing in a driven gaseous axisymmetric jet, Phys. Fluids 11 (1999) 3401–3415. doi:10.1063/1.870199.

[39] J. D. Miller, J. B. Michael, M. N. Slipchenko, S. Roy, T. R. Meyer, J. R. Gord, Simultaneous high-speed planar imaging of mixture fraction and velocity using a burst-mode laser, Appl. Phys. B: Lasers Opt. 113 (2013) 93–97. doi:10.1007/s00340-013-5665-1.

[40] J. Weinkauff, P. Trunk, J. H. Frank, M. J. Dunn, A. Dreizler, B. Böhm, Investigation of flame propagation in a partially premixed jet by high-speed-stereo-PIV and acetone-PLIF, Proc. Combust. Inst. 35 (2015) 3773–3781. doi:10.1016/j.proci.2014.05.022.

[41] M. C. Thurber, R. K. Hanson, Pressure and composition dependences of acetone laser-induced fluorescence with excitation at 248, 266, and 308 nm, Appl. Phys. B: Lasers Opt. 69 (1999) 229–240. doi:10.1007/s003409900106.

[42] M. C. Thurber, F. Grisch, B. J. Kirby, M. Votsmeier, R. K. Hanson, Measurements and modeling of acetone laser-induced fluorescence with implications for temperature-imaging diagnostics, Appl. Opt. 67 (1998) 4963–4978. doi:10.1364/AO.37.004963.

[43] V. M. Salazar, S. A. Kaiser, F. Halter, Optimizing precision and accuracy of quantitative PLIF of acetone as a tracer for hydrogen fuel, SAE Int. J. Fuels Lubr. 2 (1) (2009) 737–761. doi:10.2307/26273424.

[44] M. Stöhr, C. M. Arndt, W. Meier, Transient effects of fuel–air mixing in a partially-premixed turbulent swirl flame, Proc. Combust. Inst. 35 (2015) 3327–3335. doi:10.1016/j.proci.2014.06.095.

[45] J. Schmidt, B. Ganguly, Effect of pulsed, sub-breakdown applied electric field on propane/air flame through simultaneous OH/acetone PLIF, Combust. Flame 160 (2013) 2820–2826. doi:10.1016/j.combustflame.2013.06.031.

[46] A. M. Elbaz, W. L. Roberts, Experimental study of the inverse diffusion flame using high repetition rate OH/acetone PLIF and PIV, Fuel 165 (2016) 447–461. doi:10.1016/j.fuel.2015.10.096.

[47] W. K. Pratt, Digital Image Processing, John Wiley and Sons, Ltd, New York, NY, 1978.

[48] S. Prakash, V. Raman, C. Lietz, W. Hargus, S. Schumaker, Numerical simulation of a methane-oxygen rotating detonation rocket engine, Proc. Combust. Inst. doi:10.1016/j.proci.2020.06.288.

[49] T. Sato, V. Raman, Detonation structure in ethylene/air-based non-premixed rotating detonation engine, J. Propul. Power 36 (2020) 752–762. doi:10.2514/1.B37664.

[50] S. Prakash, R. Fiévet, V. Raman, The effect of fuel stratification on the detonation wave structure, AIAA Scitech Forum, AIAA 2019-1511, 2019. doi:10.2514/6.2019-1511.

[51] F. Chacon, M. Gamba, OH PLIF visualization of an optically accessible rotating detonation combustor, in: AIAA Propulstion and Energy Forum, AIAA 2019-4217, 2019. doi:10.2514/6.2019-4217.

[52] S. Nakagami, K. Matsuoka, J. Kasahara, Y. Kumazawa, J. Fujii, A. Matsuo, K. Funaki, Experimental visualization of the structure of rotating detonation waves in a disk-shaped combustor, J. Propul. Power 33 (2017) 80–88. doi:10.2514/1.B36084.

[53] K. Matsuoka, M. Tanaka, T. Noda, A. Kawasaki, J. Kasahara, Experimental investigation on a rotating detonation cycle with burned gas backflow, Combust. Flame 225 (2021) 13–19. doi:10.1016/j.combustflame.2020.10.048.

[54] L. Deng, H. Ma, C. Xu, C. Zhou, X. Liu, Investigation on the propagation process of rotating detonation wave, Acta Astronaut. 139 (2017) 278–287. doi:10.1016/j.actaastro.2017.07.024.

[55] R. T. M'Closkey, J. M. King, L. Cortelezzi, A. R. Karagozian, The actively controlled jet in crossflow, J. Fluid Mech. 452 (2002) 325–335. doi:10.1017/S0022112001006589.